PAPER

Real-time correction of chromatic aberration in optical fluorescence microscopy

View the article online for updates and enhancements.

Methods and Applications in Fluorescence

PAPER

Real-time correction of chromatic aberration in optical fluorescence microscopy

Ana Cayuela López[1,4] ⬩, Pablo Conesa[1,4], Ana María Oña Blanco[2], José Antonio Gómez-Pedrero[3] ⬩ and Carlos Oscar S Sorzano[1]

[1]   Biocomputing Unit, National Centre for Biotechnology, 28049 Cantoblanco, Madrid, Spain
[2]   Advanced Light Microscopy Unit, National Centre for Biotechnology, 28049 Cantoblanco, Madrid, Spain
[3]   Applied Optics Complutense Group, Faculty of Optics and Optometry, University Complutense of Madrid, 28037 Madrid, Spain
[4]   These authors contributed equally to this work.

E-mail: acayuela@cnb.csic.es, pconesa@cnb.csic.es, aoblanco@cnb.csic.es, jagomezp@fis.ucm.es and coss@cnb.csic.es

Abstract

Multi-color fluorescence imaging is a powerful tool for studying the spatial relationships and interactions among sub-cellular structures in biological specimens. However, if improperly corrected, geometrical distortions caused by mechanical drift, refractive index mismatch, or chromatic aberration can lead to lower image resolution. In this paper, we present an extension of the image processing framework of Scipion by integrating a protocol called OFM Corrector, which corrects geometrical distortions in real-time using a B-spline-based elastic continuous registration technique. Our proposal provides a simple strategy to overcome chromatic aberration by digitally re-aligning color channels in multi-color fluorescence microscopy images, even in 3D or time. Our method relies on a geometrical calibration, which we do with fluorescent beads excited by different wavelengths of light and subsequently registered to get the elastic warp as a reference to correct chromatic shift. Our software is freely available with a user-friendly GUI and can be broadly used for various biological imaging problems. The paper presents a valuable tool for researchers working in light microscopy facilities.

Abbreviations

The following abbreviations are used in this manuscript:

CA	Chromatic Aberration
ACA	Axial Chromatic Aberration
LCA	Lateral Chromatic Aberration
TIRF	Total Internal Reflection Microscopy
GUI	Graphical User Interface
IQR	Interquartile Range
FOV	Field of View
RBF	Radial Basis Functions

1. Introduction

Over the past few years, many technological advancements have been made in single molecule-based super-resolution microscopy techniques [1]. One of the imaging modalities in fluorescence microscopy is multi-color fluorescence imaging, which enables the differentiation of proteins and structures of interest in both living and fixed cells [2]. This technique also helps to determine the intracellular relationships or interactions between sub-cellular structures [1]. However, mechanical drift, chromatic aberrations caused by optical elements, refractive index mismatching between the objective and immersion medium, and dispersion in biological samples can lead to decreased image resolution [3]. In all optical systems, chromatic aberration (CA) occurs due to differences in the refractive index among optical components, causing the light wavelengths to focus at slightly different angles. The phenomenon is noticeable in the acquired images because the color channels are misaligned, causing colored fringes at the edges and high-contrast regions [4]. This can significantly decrease the image quality [5, 6]. In the case of biological applications, CA may negatively affect multi-channel studies of dynamic processes in cells, such as colocalization

research and object-based analysis. Therefore, it is essential to quantify and correct these aberrations properly. In this sense, we can find two types of CA: lateral, which occurs along the x-y axis, and axial, along the *z*-axis. Axial chromatic aberration (ACA) comes when lenses through the optics have a refractive index that varies with the wavelengths, focal distance, and image magnification. This directly affects the image focus and resolution, giving rise to image blur [7, 8]. By contrast, lateral chromatic aberration (LCA) occurs when there is variation in the magnification of different light colors. This prompts protruding image edges and deviations when two color images are superimposed.

Total Internal Reflection Fluorescence (TIRF) microscopy is a powerful optical technique to selectively acquire images of molecules in an aqueous environment with a high refractive index [9]. This approach provides extremely thin axial optical sectioning with a high signal-to-noise ratio allowing microscopists to image fluorescent membrane-associated events in living cells (cell adhesion, hormone binding, molecule transport, exocytotic and endocytotic processes, ...) as well as molecules located at the medium interface with a higher refractive index and a lower at an incidence angle bigger than critical angle [10]. The optical system may be either prism-based or objective-based to reach total internal reflection to optimize each color uniquely and independently, enabling the imaging of multiple colors simultaneously. In the first approach, a prism is attached to the coverslip's surface, which directs a focused light beam or laser toward the medium interface at the critical angle. The objective-based approach, instead, is the system mainly used, and the light is directed to the specimen through the objective, which simultaneously collects the emitted fluorescence light. In this context, dealing with multi-color and multi-angle TIRF may result challenging, and unfortunately, LCA is essentially inherent. This LCA induces shifts, rotations, and scaling differences among channels.

The Advanced Microscopy Facility of our institute has a TIRF microscope with a W-VIEW Gemini system from Hamamatsu [11], an image-splitting optics device. It was adjusted to split the signal on the camera chip by wavelength in two channels (two pairs of images) with a dichroic mirror. This optical component allows high-speed acquisition with a vast variety of fluorescence applications and permits simultaneous two-wavelength (dual) imaging by one camera due to its optical design. Additionally, this system integrates a mechanism to compensate ACA and LCA. This mechanism is based on a correction lens unit in the long wavelength path, and it can improve the magnification difference of two wavelength images caused by LCA. Furthermore, this system was designed to be easily adjusted with a camera due to integrating a fast and straightforward alignment mechanism to realign the optics. Besides that, the Gemini system has a feature to

control temperature and time stability, hence ensuring the alignment consistency of two channels over time for dual-wavelength imaging. Despite these ideal specifications, this optical component could not properly overcome the effect of LCA in our TIRF infrastructure. Interestingly, this instability is explicitly mentioned in the microscope documentation [11].

The commercial company proposed several commercial solutions (hardware- and software-based) to solve this undesirable misalignment effect. Still, most of these approaches were expensive, not intuitive at the user level, non-effective in covering the full FOV, and time-consuming. CA correction has also been addressed in the scientific literature [12]. The correction methods can be grouped into hardware- and software-based [7]. Within hardware-based methods, apochromatic lenses are developed to set into focus in the same plane, red, green, and blue wavelengths. Also, active lens control systems are designed [13] to correct CA by adjusting the distance between the image plane and lens. Nevertheless, apochromatic lenses are affected by residual errors too big to be ignored, and the lens control system requires prior knowledge of the magnification and image shift degree. On the other hand, most software-based methods to compensate CA are based on image registration [14], false color techniques [15], and post-demosaicking correction based on pixel re-sampling and high-pass replication [16]. However, none of these methods are readily available and easily integrated within the standard procedures of a microscopy facility.

In this paper, we use image registration to compensate the geometrical distortions induced by LCA. This technique works by spatially registering images such that corresponding features are consistent in geometry. It involves identifying corresponding features or pixels in two or more images and then applying a geometric transformation to align them. The transformation can be rigid, affine, or non-rigid, depending on the type and degree of misalignment. This paper uses B-spline-based elastic image registration [17] for modeling deformations in biological imaging problems [18]. This technique has several advantages, such as coping with a wide range of deformations, including non-linear [17]. The registration process is based on image similarity, deformation consistency, and cubic B-spline regularization [19]. This technique ensures high-quality interpolation of the images and allows an arbitrarily fine representation of the deformation field by reducing the spacing among splines. B-spline-based elastic image registration is advantageous in many biological imaging problems, such as tracking the movement of cells or analyzing the shape of tissues. Accordingly, B-spline based methods have gained popularity in image registration due to their flexibility and ability to accurately capture complex deformations. Among its advantages, this approach allows for localized control over the deformation field by dividing the image into smaller regions (control points)

thus, representing localized deformations more effectively. This can be advantageous when dealing with complex and non-uniform deformations, which can vary spatially across the image. Moreover, B-spline method provides smooth and continuous deformations, something particularly relevant in microscopy, where smooth deformations are desirable to preserve anatomical structures or avoid introducing artifacts. B-spline methods are computationally attractive, which is especially worthy when dealing with large image datasets or real-time approaches. On the other hand, alternative methods such as radial basis functions (RBF) with compact support, also provide accurate deformations, particularly for small and localized deformations with high precision. While RBF methods are widely used for their interpolation properties which can capture fine details exactly, they are still challenging handling large deformations or global registration tasks due to the compact support limitation. Therefore, the choice of the most suitable registration method over alternative approaches depends on the specific requirements of the application, the study context, the nature of the deformations and the available computational resources. For such, the B-spline-based method was selected for this study based on its ability to handle complex deformations, provide smooth results as well as efficient computation.

Our method utilizes multispectral fluorescent beads as a reference for image registration and drift correction [20]. These fluorescent beads are excited by different wavelengths of light and emit differently in the same wavelength range as the applied dyes. The shift between image channels is recorded and registered for the warp transformation to correct further chromatic shifts in images acquired under the same imaging setup. This elastic registration process involves finding the image transformation that can best map one image into the other. The integrated algorithm extends the elastic (non-linear) registration approach [17] by providing an almost invertible deformation field, allowing bidirectional registration. This ensures that source image A can be mapped onto target image B and vice versa in a single computation, thereby reducing the optimizer likelihood of being trapped in a local minimum and enabling simultaneous registration of any number of images.

A requirement for facilities is that the solution must work in real-time while the TIRF videos are acquired. This way, the user can bring home the CA-corrected data after finishing the microscopy session. To this end, we have developed a protocol called *ofmcorrection - OFM Corrector* based on the bUnwarpJ [19, 21] plugin (available under ImageJ [22] or Fiji [23] distribution) and integrated into the Scipion's image processing framework [24]. Before acquiring the TIRF videos, the microscope operator must calibrate the deformation field for that particular acquisition (because the deformation field depends on the ambient temperature, the specific magnification setup, and the Field of View (FOV) region being imaged). Once calibrated, the deformation field is used to correct all the videos acquired with the same conditions. Our protocol offers a unified graphical user interface (GUI), package interoperability, a simple and cost-effective strategy to overcome geometrical distortions, and workflow monitoring for the streaming registration process (see figure 1). Our software is freely available within Scipion framework and can be used in any microscopy setup with geometric distortions affecting the acquired videos.

2. Real-time correction of geometric distortions

This section describes the algorithmic approach to solving geometric distortions. We first introduce the procedure to measure the geometric distortions at the microscope experimentally. Then, we describe our algorithm to construct a mathematical description of the deformation field and correct it. Finally, we present the framework that allows real-time correction with images in streaming.

2.1. Experimental measure of the deformation field
A possible way to experimentally measure the deformation field is by recording images of known objects. Multi-spectral fluorescent beads are suitable for this purpose because they fluoresce at various wavelengths, and any image misalignment can be easily detected [25]. Figure 2 shows the conceptual setup from one of our experiments. The various wavelengths are projected differently by the dichroic mirror, so the image of the same bead is projected at two different locations. From a pair of these images, we can estimate the relative deformation field ($\mathbf{g}^{12}(\mathbf{s})$ in the equation (1) below).

As shown in figure 2(D), we can see that the LCA shift depends on the region of the FOV being imaged and the lateral distance to the center of the image.

2.2. Elastic image registration
Let us consider a pair of images acquired in Channels 1 and 2, $I^1(\mathbf{s})$ and $I^2(\mathbf{s})$, where $\mathbf{s} = (x, y)$ is a 2D vector with the pixel coordinate. Elastic image registration assumes that there is a deformation field, $\mathbf{g}^{12}$, that transforms coordinates from one channel onto the coordinates of the other:

$$I^1(\mathbf{s}) = I^2(\mathbf{s} + \mathbf{g}^{12}(\mathbf{s})) \tag{1}$$

In case there is no geometrical distortion, then $\mathbf{g}^{12}(\mathbf{s}) = \mathbf{0}$ for all $\mathbf{s}$, and the two channels should superpose exactly. However, if they do not, we look for the deformation field that minimizes the error between these two images. To estimate the deformation field, it is important to use objects whose emission in both channels is the same (see the previous section).
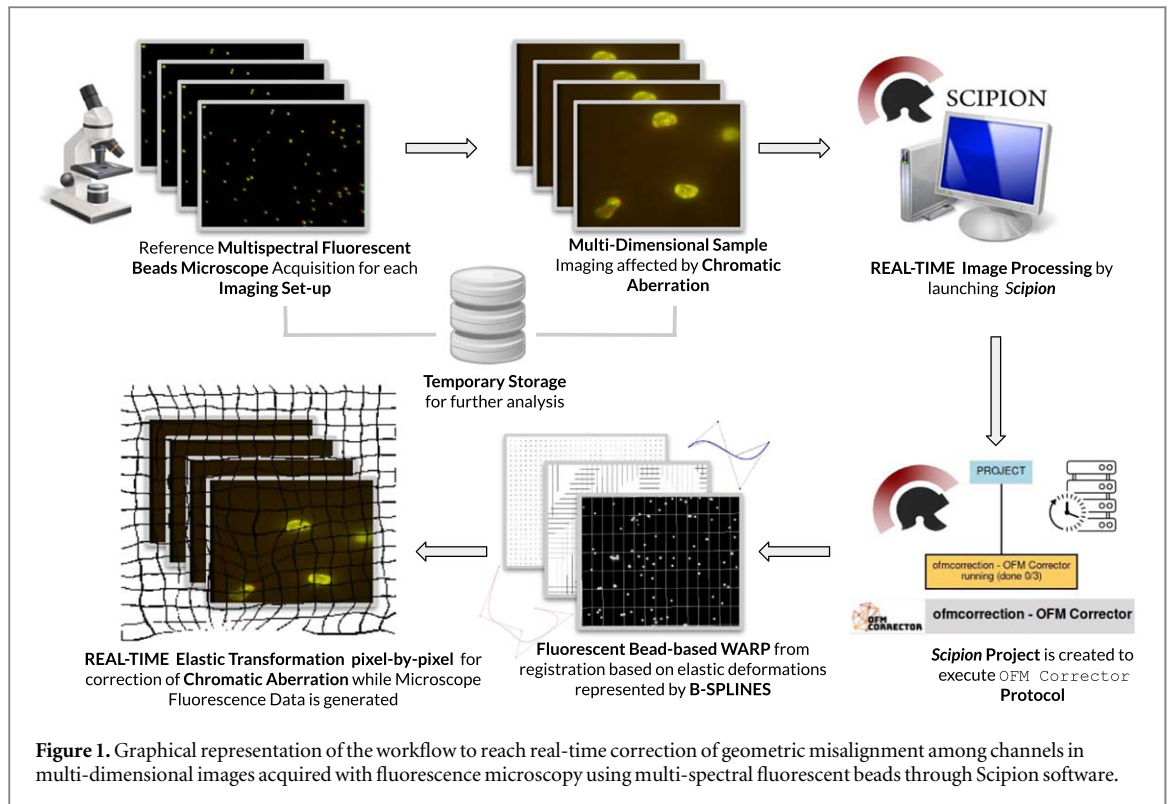
Figure 1. Graphical representation of the workflow to reach real-time correction of geometric misalignment among channels in multi-dimensional images acquired with fluorescence microscopy using multi-spectral fluorescent beads through Scipion software.
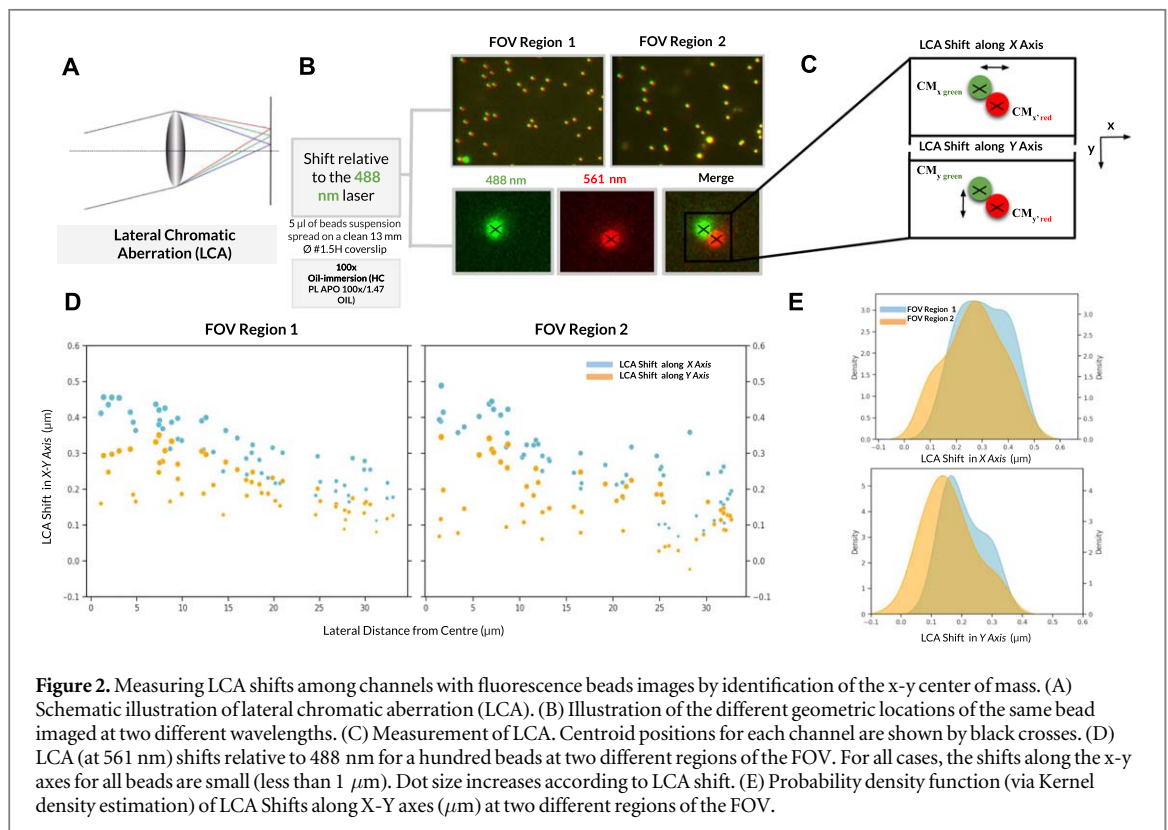

Figure 2. Measuring LCA shifts among channels with fluorescence beads images by identification of the x-y center of mass. (A) Schematic illustration of lateral chromatic aberration (LCA). (B) Illustration of the different geometric locations of the same bead imaged at two different wavelengths. (C) Measurement of LCA. Centroid positions for each channel are shown by black crosses. (D) LCA (at 561 nm) shifts relative to 488 nm for a hundred beads at two different regions of the FOV. For all cases, the shifts along the x-y axes for all beads are small (less than 1 μm). Dot size increases according to LCA shift. (E) Probability density function (via Kernel density estimation) of LCA Shifts along X-Y axes (μm) at two different regions of the FOV.

We use a B-splines parametrization of the deformation field as explained in [17]. This way, the deformation field is calculated as

$$\mathbf{g}^{12}(\mathbf{s}) = \sum_{ij} \mathbf{c}_{ij}^{12} B\left(\frac{x - ih}{h}\right) B\left(\frac{y - jh}{h}\right) \quad (2)$$

where i and j are indexes over a regular lattice of B-spline functions, B, whose separation between grid points is h is both directions. The coefficients $\mathbf{c}_{ij}^{12} \in \mathbb{R}^2$ are the ones that control the amount of deformation in x and y.

The transformation $\mathbf{g}^{12}(\mathbf{s})$ may not be invertible. It has been observed that this deformation field is better
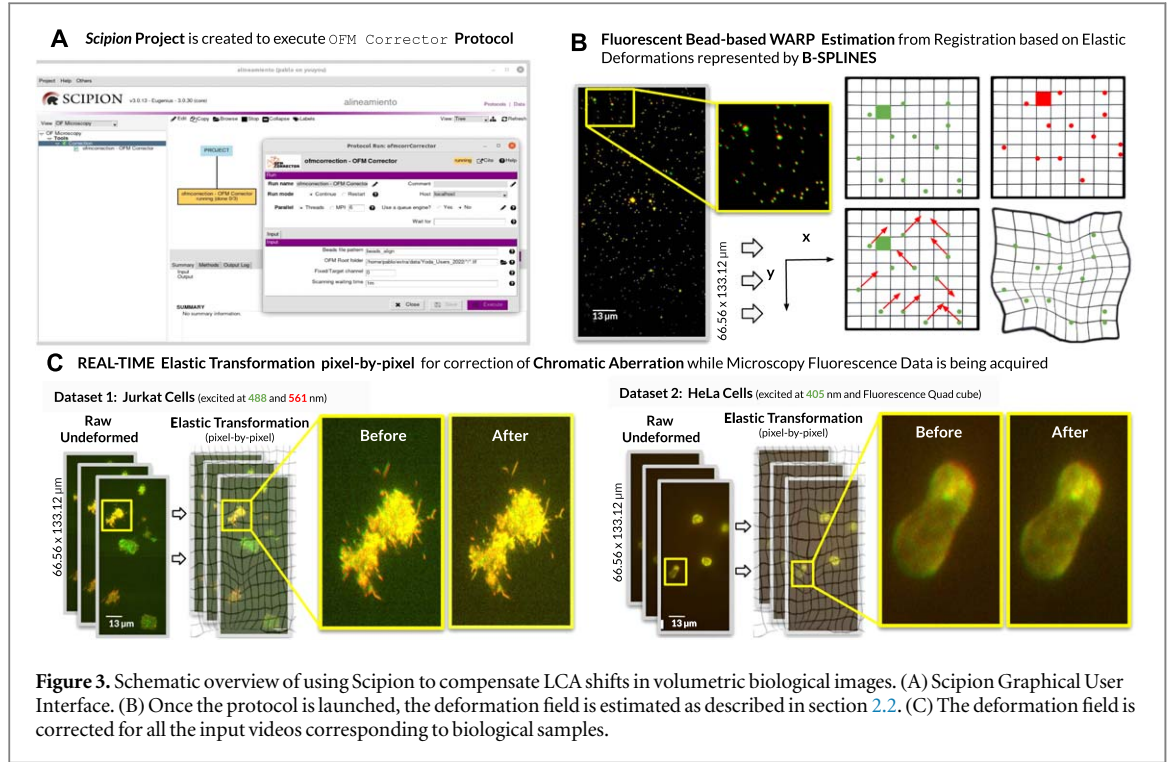
Figure 3. Schematic overview of using Scipion to compensate LCA shifts in volumetric biological images. (A) Scipion Graphical User Interface. (B) Once the protocol is launched, the deformation field is estimated as described in section 2.2. (C) The deformation field is corrected for all the input videos corresponding to biological samples.

estimated if the deformation is computed bidirectionally:

$$I^1(\mathbf{s}) = I^2(\mathbf{s} + \mathbf{g}^{12}(\mathbf{s}))$$
$$I^2(\mathbf{s}) = I^1(\mathbf{s} + \mathbf{g}^{21}(\mathbf{s})) \qquad (3)$$

and $\mathbf{g}^{12}$ and $\mathbf{g}^{21}$ are supposed to be approximate inverses of each other:

$$\mathbf{g}^{21}(\mathbf{g}^{12}(\mathbf{s})) \approx \mathbf{s} \qquad (4)$$

This approximate inverse condition is called a consistency constraint.

The $\mathbf{c}_{ij}^{12}$ and $\mathbf{c}_{ij}^{21}$ coefficients are determined by minimizing the following error function

$$E = \sum_{\mathbf{s}} \|I^1(\mathbf{s}) - I^2(\mathbf{s} + \mathbf{g}^{12}(\mathbf{s}))\|^2 + \sum_{\mathbf{s}} \|I^2(\mathbf{s})$$
$$-I^1(\mathbf{s} + \mathbf{g}^{21}(\mathbf{s}))\|^2 \qquad \text{image dissimilarity}$$
$$+w_c \sum_{\mathbf{s}} \|\mathbf{g}^{21}(\mathbf{g}^{12}(\mathbf{s})) - \mathbf{s}\|^2$$

consistency error

$$+w_d \left(\sum_{\mathbf{s}} (\|\nabla \mathrm{div}\mathbf{g}^{12}(\mathbf{s})\|^2 + \|\nabla \mathrm{div}\mathbf{g}^{21}(\mathbf{s})\|^2) \right)$$

regularization divergence

$$+w_r \left(\sum_{\mathbf{s}} (\|\nabla \mathrm{rot}\mathbf{g}^{12}(\mathbf{s})\|^2 + \|\nabla \mathrm{rot}\mathbf{g}^{21}(\mathbf{s})\|^2) \right)$$

regularization rotational

$$(5)$$

where w_c, w_d, and w_r are weights that control the relative weight of the different terms The minimization of the error term with respect to the B-spline coefficients was explained in [19, 21], and it is publicly available through the BUnwarpJ plugin of ImageJ. We have not reimplemented this algorithm, but we call it through Fiji.

We estimate the deformation field, which is encoded through the $\mathbf{c}_{ij}^{12}$ and $\mathbf{c}_{ij}^{21}$ coefficients, during the calibration step. These coefficients are saved after calibration and reused to produce aligned images. For instance, to correct the image from Channel 2 so that it is registered with Channel 1, we construct the image $(I^2)'$ as

$$(I_t^2)'(\mathbf{s}) = I_t^2(\mathbf{s} - \mathbf{g}^{12}(\mathbf{s})) \qquad (6)$$

The subindex t has been introduced to represent the different time frames within a video. The distortion correction above is applied to all the video frames acquired by the TIRF microscope.

2.3. Geometric corrections in real-time

Microscopy facilities continuously receive users acquiring their images on the samples of their interest. In this scenario, it is essential for facilities to keep up to the highest quality standard. Having a microscope with severe geometrical distortions, such as the one presented in this paper, is a drawback for the facility. Therefore, we have integrated the elastic registration algorithm described above into an image-processing workflow engine called Scipion [24]. This workflow engine is also developed by our laboratory. This engine allows image processing in streaming [26]: the newly acquired images are geometrically corrected as soon as they are written in their folder (see figure 3). In this way, the user can bring home the already corrected images. The plugin is called *ofmcorrection* and the protocol *OFM Corrector*. The beads images are one of the inputs of the protocol. The protocol first estimates the deformation field to correct. Then it applies it to all videos in the input folder (it must be noted that this

correction is applied on-the-fly, so new videos can arrive once the protocol has started). The geometrical distortion corrected is the same for all videos and is measured at the beginning of the acquisition as described in section 2.1. This calibration image is only valid for experimental images acquired under the same exposure time, camera gain, region of the field of view, brightness, photo-stability, temperature, and ambient light in the facility.

3. Materials and methods

3.1. Code availability
OFM Corrector protocol was written in Groovy and integrated into Scipion framework by using Python. The complete source code of the algorithm integrated in Scipion software is available at https://github.com/acayuelalopez/bUnwarpJ_code. Our protocol can be used for real-time processing within the Scipion framwork. You can install it by using the Scipion software following the Scipion's installation guide (https://scipion-em.github.io/docs/release-3.0.0/docs/scipion-modes/how-to-install.html).

3.2. Experimental methods
3.2.1. Calibration sample preparation
Multispectral fluorescent beads suspension (Tetra-Speck^{TM} Microspheres, 0.2 μm, fluorescent blue/green/orange/dark red, TermoFisher Scientific) were used as a reference for calibration of the image alignment. Five microlitres of the beads suspension were pipetted and spread on a clean 13 mm Ø #1.5H coverslip (Menzel Gläser) for 1 hour for adhesion to the glass. The coverslip was placed on a slide and sealed with enamel. Once the sample beads were prepared, they were placed on the immersion oil objective (Leica^{TM} Immersion Oil) of the TIRF microscope to acquire several images. The fluorescent beads were simultaneously excited by two different wavelengths of light: 488, and 561 nm lasers. In our acquisition, we used a 100x oil-immersion objective (HC PL APO 100x/1.47 OIL) with a Leica DMi8 S with TIRF module microscope equipped with Hamamatsu Flash 4 digital sCMOS camera.

3.2.2. Biological sample preparation
Jurkat cells (American Type Culture Collection, ATCC TIB-152) or HeLa cells (ATCC CCL-2) were maintained in culture using a complete growth medium (RP 1640 or DMEM, Gibco, plus 10% fetal calf serum) at 37 °C and 5% CO_2.

Jurkat cells were transiently transfected with plasmids to express cell membrane receptors fused to EGFP or mCherry reporters using a BioRad electroporator (2×10^4 cells in RP 1640 with 10% fetal calf serum. 280V, 975 mF) and imaging 24 hours later.

DNA Hela cells were stained 10 minutes with Hoechst 33342 (ThermoFisher Scientific) at 0.5 mg/mL prepared in cell culture medium. The staining solution was gently removed and the cells were washed with culture medium to remove unbound dye. To proceed with image acquisition, the cells were left in DMEM medium plus 10% fetal calf serum. For the imaging experiments, the cells were seeded in a μ-Dish 35 mm, high glass bottom dish (Ibidi) at a density of 20,000 to 50,000 cells per well.
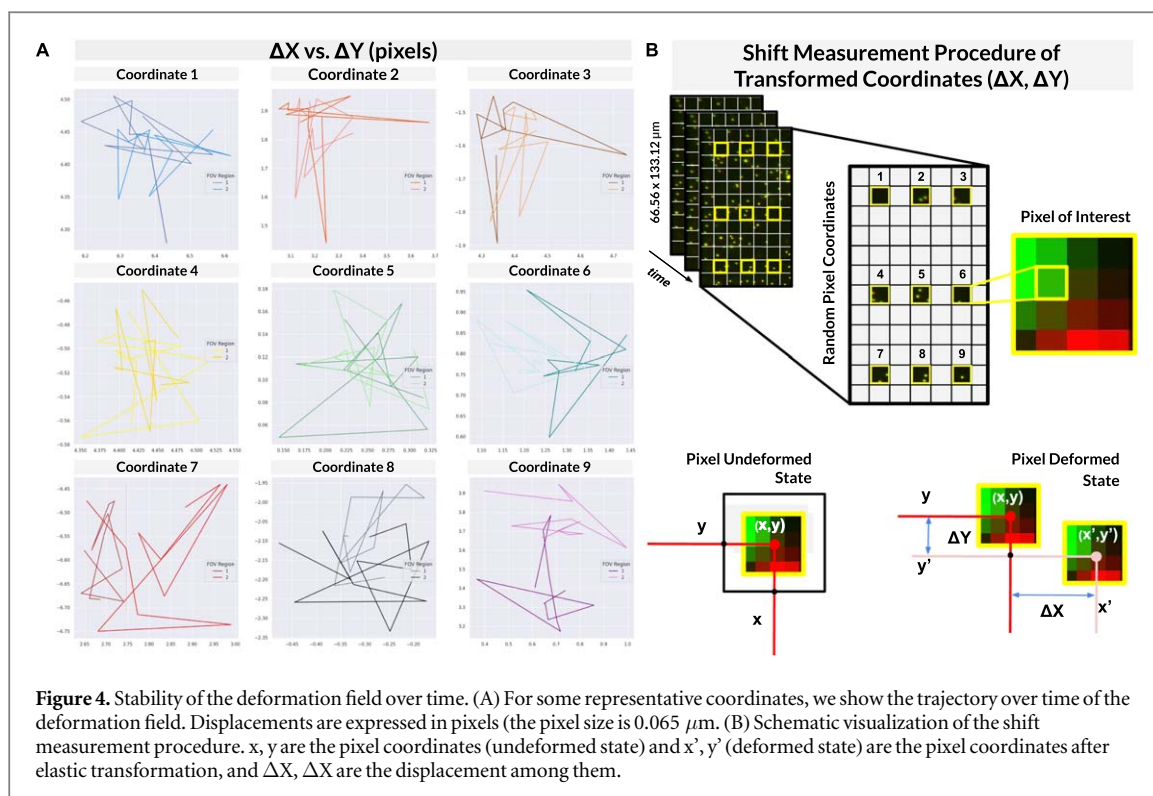
3.2.3. Dual TIRF imaging
Dual TIRF experiments were performed using a Leica DMi8 S with a TIRF module microscope equipped with a Hamamatsu Flash 4 digital sCMOS camera (Hamamatsu), a 100x oil-immersion objective (HC PL APO 100x/1.47 OIL), and the 405, 488 and 561 nm laser lines for the illumination of the samples. Two types of W-View Gemini splitter (Hamamatsu) were used for simultaneous image acquisition. This image-splitting optic provides a pair of dual-wavelength or polarization images separated by a dichroic mirror in a single camera. The beam divider allowed us to obtain two separate sample images of the same field of view (FOV) on the same camera chip. When the W-View optics were in place, the Hamamatsu W-View Gemini option was activated in the software interface, and the images of the simultaneously imaged beads were manually aligned to correct the focus, zoom, and x and y shift between the two channels using EPI laser position (without laser penetration depth). Once manually aligned, the reference images were acquired with an EPI laser position. Then, the images were acquired with the biological sample under the acquisition conditions required by the experimental design. The microscope was equipped with an incubator and temperature control units; experiments were performed at 37 °C with 5% CO2. Z-stabilization was ensured by the adaptive focus control (AFC) on the microscope.

Image sequences (500 frames for Jurkat cells and 11 frames for HeLa cells) were acquired with a 90 ms/frame rate for Jurkat cells and 60 ms/frame for HeLa cells. The penetration depth of the evanescent wave was 90 nm for Jurkat cells and EPI laser position for HeLa cells. The images have 512×1024 (0.13 $\times$ 0.13 μm pixel size) for Jurkat cells or 1024×2048 (0.065 $\times$ 0.065 μm pixel size) pixels for HeLa cells and were acquired at 16-bit.

For EGFP/mCherry imaging, the 488 and 561 nm excitation lasers lines were used simultaneously, and the fluorescence Dual cube (GFP/Ch-T) employed has excitation filters between 483-493 and 550-568 nm, an emission filters between 507-553 and LP575 nm and dichromatic beamsplitters at 500 and 575 nm. The bandpass filters used were for GFP/DsRED dual-band imaging set (FF01-512/25-25, FF01-630/92-25, and dichroic mirror FF560-FDi01-25 $\times$ 36).

For Hoechst 33342 imaging, the 405 excitation laser was used with the fluorescence Qua-T cube. The

Figure 4. Stability of the deformation field over time. (A) For some representative coordinates, we show the trajectory over time of the deformation field. Displacements are expressed in pixels (the pixel size is 0.065 μm. (B) Schematic visualization of the shift measurement procedure. x, y are the pixel coordinates (undeformed state) and x', y' (deformed state) are the pixel coordinates after elastic transformation, and ΔX, ΔX are the displacement among them.

Qua-T cube has an excitation filter between 397–413 nm, an emission filter between 420–480 and 500–550 nm, and dichromatic beamsplitters at 415 and 495 nm, respectively, among others.

4. Results

We started by estimating and characterizing the deformation field and its stability over time. Then, we applied our method to two biological data sets consisting of dual-wavelength images acquired with two different z-axis depths (described in detail in section 3.2.2).

4.1. Stability of the deformation field over time
We acquired images of the beads exited with two laser channels, 488 and 561 nm., every hour during the day (12 measures in total). We focused the microscope on two different regions of the FOV. We estimated the deformation field and evaluated its stability in every location. Figure 4 shows the trajectories over time of the x and y components of $\mathbf{g}^{12}(\mathbf{s})$ (figure 4(A)) for 9 points uniformly distributed over the region being imaged (figure 4(B)).

Depending on the FOV region and the location within this region, the deformation field can be as high as 6.6 pixels (about 0.4 μm., figure 4(A)), or even higher for pixels closer to the image border. In the center of the region, figure 4(E), the deformation is relatively small. For this reason, that was the only area that the microscope users used to analyze before the facility incorporated our real-time correction. To facilitate the visualization over the whole region, in figure 5, we
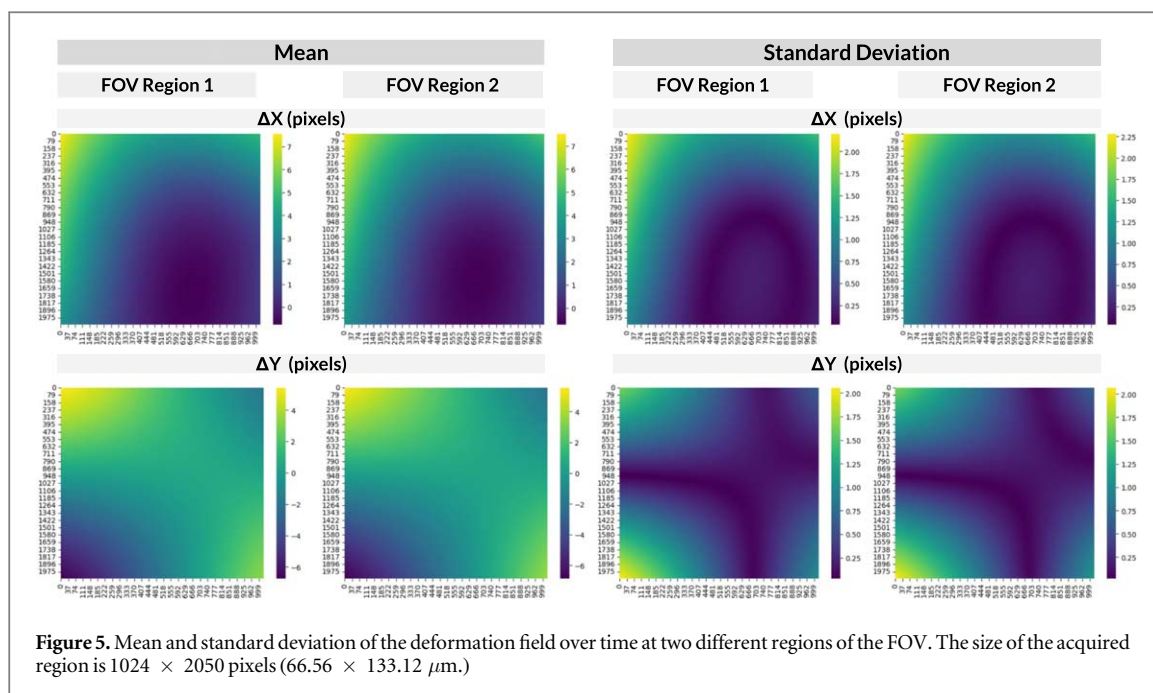
show the mean and standard deviation of the deformation field over time at every location for two different regions. Interestingly, the vertical and horizontal distortions behave differently. This is due to the polarization of the light being used and the possible anisotropic nature of the crystals of which the different optical devices along the path are made.

4.1.1. Dataset 1: jurkat cells
This dataset consists of four series containing 1000 planes with a voxel size of $0.13 \times 0.13 \times 1 \, \mu$m^3 saved as Leica File Format (figure 3(C), top). Jurkat cells were transiently transfected, expressing cell membrane receptors fused to EGFP (green, 488 nm.) or mCherry (red, 561 nm.) reporters. Two simultaneously acquired image sequences (500 frames) GFP/DsRED dual-band imaging filters were used. The sample was illuminated with 488 and 561 nm. laser lines and fluorescence dual cube was used. The images were acquired with a frame rate of 90 ms/frame, and the penetration depth of the evanescent wave was 90 nm. The images were acquired with a pixel map of 512×1024 pixels ($66.56 \times 133.12 \, \mu$m) and a bit-depth of 16 bits. As shown in figure 3(C), the raw images are heavily affected by LCA. After applying the bead-based warping transformation, LCA misalignment was always fully corrected (500 frames).

4.1.2. Dataset 2: HeLa cells
This dataset consists of 6 series containing 22 planes with a voxel size of $0.13 \times 0.13 \times 1 \, \mu$m^3 saved as Leica File Format (figure 3(C), bottom). The nuclei of HeLa cells were stained with Hoechst 33342. Two

Figure 5. Mean and standard deviation of the deformation field over time at two different regions of the FOV. The size of the acquired region is 1024 $\times$ 2050 pixels (66.56 $\times$ 133.12 μm.)

simultaneously acquired image sequences (11 frames) light polarization filters set were used. The sample was illuminated with a 405 nm. laser line and a fluorescence Quad cube was used. The images were acquired with a 60 ms/frame rate and EPI laser position. The pixel size and bit-depth of the acquired images were the same as in the previous dataset. As seen in figure 3(C), the misalignment caused by LCA was also corrected following the same procedure as in the previous dataset.

5. Discussion and conclusions

Chromatic aberration is a prevalent issue in multi-color imaging. However, geometric distortions may appear for other experimental reasons, such as imperfections of the optical elements, the mismatch between the refractive index of the objective and immersion medium, or differential dispersion inside the biological samples. We have developed an inexpensive and very efficient solution to a problem that the company commercializing the microscope could not solve with a more accurate physical construction of the dichroic mirror. This problem severely limited the region the microscope users could analyze in their biological experiments. Our software solution is integrated into a protocol called the *OFM Corrector*, freely accessible within the Scipion framework. Scipion offers the possibility of applying the geometrical correction in streaming and real-time, providing almost instant aberration-corrected images. This way, our solution favorably compares to expensive optical solutions. Additionally, it is much more general as it does not only address chromatic aberration but any other source of geometrical distortions. This method can be applied easily to all future acquisitions in the light

microscopy facility by capturing a reference calibration image for each condition. This calibration step depends on the specific imaging set-up, including excitation laser lines, objective lens, temperature stability, and exposure time. Also, selecting the most suitable multi-spectral fluorescent beads based on their signal and size is vital to ensure that the bead diameter is reasonably above the microscope's resolution, providing a sufficient signal-to-noise ratio. Our solution is not limited to correcting geometrical distortions between two channels. Any number of channels can be simultaneously corrected. One of the channels must act as the reference channel, while all the others are corrected to match the reference.

Overall, this protocol has the potential to be widely adopted in light microscopy facilities and carries significant implications for the field of biological imaging. Future efforts may concentrate on expanding the protocol's capabilities to address additional optical distortions found in biological imaging.

Author contributions

ACL, PCM, JAGP, and COSS conceived the project and designed the algorithms. ACL and PCM wrote the software code and performed all experiments. AOB prepared the samples and acquired the images at the

microscope. All authors have read and agreed to the published version of the manuscript. All authors have read and agreed to the published version of the manuscript.

Funding

Conflicts of interest

The authors declare no conflict of interest.

ORCID iDs

Ana Cayuela López ⓘ https://orcid.org/0000-0001-7728-9867
José Antonio Gómez-Pedrero ⓘ https://orcid.org/0000-0001-7043-3256

References

[1] Tam J, Cordier G A, Borbely J S, Sandoval Álvarez Á and Lakadamyali M 2014 Cross-talk-free multi-color storm imaging using a single fluorophore *PLoS One* **9** 7
[2] Dean K and Palmer A 2014 Advances in fluorescence labeling strategies for dynamic cellular imaging *Nat. Chem. Biol.* **10** 7
[3] Matsuda A, Schermelleh L, Hirano Y, Haraguchi T and Hiraoka Y 2018 Accurate and fiducial-marker-free correction for three-dimensional chromatic shift in biological fluorescence microscopy *Sci. Rep.* **8** 1
[4] Rudakova V and Monasse P 2014 Precise correction of lateral chromatic aberration in images *Image and Video Technology* ed R Klette *et al* (Berlin Heidelberg: Springer Berlin Heidelberg) pp 12–22
[5] Yu H, Zhou Z, Qi Y, Zhang X and Wei Q H 2019 Pancharatnam-berry optical lenses *J. Opt. Soc. Am.* B **36** 107–11
[6] Yousefzadeh C, Jamali A, McGinty C and Bos P J 2018 Achromatic limits of pancharatnam phase lenses *Appl. Opt.* **57** 1151–8
[7] Huang J, Xue Q, Wang Z and Gao J 2016 Analysis and compensation for lateral chromatic aberration in a color coding structured light 3d measurement system *Sensors* **16** 9
[8] Leiwe M N, Fujimoto S and Imai T 2021 Post hoc correction of chromatic aberrations in large-scale volumetric images in confocal microscopy *Frontiers in Neuroanatomy* **15** 760063
[9] Axelrod D 2001 Total internal reflection fluorescence microscopy in cell biology *Traffic* **2** 764–74
[10] Fish K N 2009 Total internal reflection fluorescence (TIRF) microscopy *Current Protocols in Cytometry* **50** 12.18.1–12.18.13
[11] Hamamatsu Photonics K K W-VIEW GEMINI Image Splitting Optics A12801-01 Technical Note, https://hamamatsu.com/content/dam/hamamatsu-photonics/sites/documents/99_SALES_LIBRARY/sys/SBIS0101E_A1280101.pdf
[12] Roberts D, Liao Z, Hwang J Y, Nersisyan S R, Tabirian N, Steeves D M, Kimball B R and Bunning T J 2018 Chromatic aberration corrected switchable optical systems *Liquid Crystals XXII* ed I C Khoo (International Society for Optics and Photonics, SPIE) vol 10735 107350Q
[13] Willson R G and Shafer S A 1991 Active lens control for high precision computer imaging *Proceedings. 1991 IEEE International Conference on Robotics and Automation, vol 3* pp 2063–70
[14] Lluis-Gomez A and Edirisinghe E A 2012 Chromatic aberration correction in raw domain for image quality enhancement in image sensor processors *2012 IEEE VIII International Conference on Intelligent Computer Communication and Processing* pp 241–4
[15] Chang J, Kang H and Kang M G 2013 Correction of axial and lateral chromatic aberration with false color filtering *IEEE Trans. Image Process.* **22** 1186–98
[16] Korneliussen J T and Hirakawa K 2014 Camera processing with chromatic aberration *IEEE Trans. Image Process.* **23** 4539–52
[17] Sorzano C O S, Thévenaz P and Unser M 2005 Elastic registration of biological images using vector-spline regularization *IEEE Trans. Biomed. Eng.* **52** 652–63
[18] Uji A, Ooto S, Hangai M, Arichika S and Yoshimura N 2013 Image quality improvement in adaptive optics scanning laser ophthalmoscopy assisted capillary visualization using b-spline-based elastic image registration *PLoS One* **8** 11
[19] Arganda-Carreras I, Sorzano C O S, Marabini R, Carazo J M, Ortiz-de C, Solorzano and Kybic J 2006 Consistent and elastic registration of histological sections using vector-spline regularization *Lect. Notes Comput. Sci.* **4241** 85–95
[20] Erdelyi M, Rees E, Metcalf D, Kaminski Schierle G S, Dudas L, Sinko J, Knight A E and Kaminski C F 2013 Correcting chromatic offset in multicolor super-resolution localization microscopy *Opt. Express* **21** 10978–88
[21] Arganda-Carreras I, Sorzano C O S, Kybic J and Ortiz de Solorzano C 2008 bunwarpj: Consistent and elastic registration in imagej. methods and applications *ImageJ Conference Users-Developers*
[22] Schneider C, Rasband W and Eliceiri K 2012 NIH image to imagej: 25 years of image analysis *Nat. Methods* **9** 7
[23] Schindelin J *et al* 2012 Fiji: An open-source platform for biological-image analysis *Nat. Methods* **9** 676–82
[24] de la Rosa-Trevin J M *et al* 2016 Scipion: A software framework toward integration, reproducibility and validation in 3d electron microscopy *J. Struct. Biol.* **195** 93–9
[25] Jorge-Peñas A, Izquierdo-Alvarez A, Aguilar-Cuenca R, Vicente-Manzanares M, Garcia-Aznar J M, Van Oosterwyck H, de Juan-Pardo E M, Ortiz-de Solorzano C and Muñoz-Barrutia A 2015 Free form deformation-based image registration improves accuracy of traction force microscopy *PLoS One* **10** 12
[26] Maluenda D *et al* 2019 Flexible workflows for on-the-fly electron-microscopy single-particle image processing using scipion *Acta Crystallographica Section D: Structural Biology* **75** 882–94